

Study on Process Optimization of Cold Gas Spraying

H. Tabbara, S. Gu, D.G. McCartney, T.S. Price, and P.H. Shipway

(Submitted April 23, 2010; in revised form September 14, 2010)

Cold gas dynamic spraying is a relatively new spray coating technique capable of depositing a variety of materials without extensive heating. As a result the inherent degradation of the powder particles found during traditional thermal spraying can be avoided. The simplicity of this technique is its most salient feature. High pressure gas is accelerated through a convergent-divergent nozzle up to supersonic velocity. The powder particles are carried to the substrate by the gas and on impact the particles deform at temperatures below their melting point. Computational modeling of thermal spray systems can provide thorough descriptions of the complex, compressible, particle-laden flow, and therefore can be utilized to strengthen understanding and allow technological progress to be made in a more systematic fashion. The computational fluid dynamic approach is adopted in this study to examine the effects of changing the nozzle cross-section shape, particle size and process gas type on the gas flow characteristics through a cold spray nozzle, as well as the spray distribution and particle velocity variation at the exit.

Keywords 3D, CFD, cold spray, convergent-divergent nozzle, helium

1. Introduction

Developed in the mid-1980s at the Russian Academy of Science (Ref 1), cold gas dynamic spraying (CGDS) is a relatively new spray coating technique. From the outset it was demonstrated that pure metals, metal alloys, and composite powders can be deposited without extensive heating. As a result the inherent degradation of the powder particles due to overheating, which are commonly found in traditional, high-temperature thermal spraying can be largely reduced. These include: high-temperature oxidation, phase changes, crystallization, and residual tensile stresses due to solidification shrinkage (Ref 1, 2).

CGDS is renowned for its simplicity. High pressure gas is accelerated through a de Laval nozzle, and depending on the type of gas, pressure, and temperature the gas velocity can exceed 1000 m/s. The powder particles which range in size from 1 to 50 μm (Ref 1) are accelerated to the substrate by the gas at temperatures below their melting point. In order to achieve adhesion on impact the particles deform in their solid state, characterized by high strain rates through the material (Ref 3). The particle velocity on impact is one of the dominant factors con-

trolling the deposition efficiency (Ref 4). It has been shown that when a critical velocity (v_c) is exceeded adiabatic shear instabilities form (Ref 5, 6). This process involves heat release on impact due to deformation at the interface between the particle and the impingement zone, which induces further thermal softening and in turn induces viscous-like flow (Ref 7). This unstable plastic deformation is the dominant mechanism in the bonding between the particle and the substrate in cold spray (Ref 8). v_c can be equated to the relative densities of the particle and the substrate, and further relies on their thermal and mechanical properties (Ref 5, 9). However, if v_c is not exceeded and the particle fails to deform to an adequate degree erosion at the surface may take place, or the particle may rebound from the surface, creating material waste and heightened turnaround times.

Computational modeling is becoming ubiquitous within experimental thermal spray research, allowing thorough descriptions of the complex, compressible, multiphase flows to be built. By applying these methods to cold spray an in-depth knowledge and understanding of the particle-laden flow can be built and technological progress can be made in a more systematic fashion. In fact several computational fluid dynamic (CFD) models have been utilized in the development of cold spray, and due to the common cold spray nozzle having a circular cross-section the majority of these studies adopt a two-dimensional axisymmetric domain. Among these, investigations include geometric optimization of the de Laval nozzle by varying the length and expansion-ratio (Ref 10-12) as well as testing the effects of stand off distance and the bow shock phenomena on particle impact velocity (Ref 4, 13). Powder particle velocity has also been shown to be affected by the particle size (Ref 4, 10, 12-14) and the type of material being sprayed (Ref 4, 13-15).

Several research papers have been targeted at optimizing the geometry of conical nozzles, including (Ref 10-12).

H. Tabbara, and S. Gu, Energy Technology Research Group, School of Engineering Sciences, University of Southampton, Highfield, Southampton SO17 1BJ, UK; and D.G. McCartney, T.S. Price, and P.H. Shipway, Department of Mechanical, Materials and Manufacturing Engineering, University of Nottingham, University Park, Nottingham NG7 2RD, UK. Contact e-mail: s.gu@soton.ac.uk.

However, there have been few steps taken to investigate the possibility of designing a more complex contour shape. Some early work undertaken by Dykhuizen et al. (Ref 2) to optimize the nozzle cross-sectional area through the coupling of the isentropic flow equations and the particle drag force was conducted in one dimension.

In this investigation the method of characteristics (MOC) is applied to test a minimum length, two-dimensional de Laval nozzle with a contoured diverging section. Its performance is numerically simulated and compared alongside an equivalent conical design with nitrogen as the process gas at a stagnation pressure and temperature of 3 MPa and 300 K. 11 μm copper particle is tracked through the gas phase along the centerline and their dynamic response is viewed for both the conical and the contoured scenarios.

A small amount of 3D CFD modeling has been applied previously to cold spray (Ref 16), which successfully simulates the compressible flow through a de Laval nozzle. However, this study is without nozzle design development and lacks vigorous scientific discussion. The investigation is focused on the novel development of a CFD tool for numerically simulating and then postprocessing and visualizing particle concentrations outside of the nozzle. The computational time and resource required to produce a realistic 3D model is limiting the depth of research in this field. In particular 2D models are unable to simulate a realistic particle distribution, and design developments have to exclude cross-section shape variation. In order to tackle this current barrier full 3D models are constructed for investigation and are used to simulate the particle-laden flow through various cold spray nozzles. The models

are utilized to investigate the particle distributions at the nozzle exit for nitrogen and helium gas flow and for different size particles. Furthermore, circular, square, and elliptical nozzle cross sections are simulated to test their effect on the particle dynamic response.

In summary, the CFD approach is applied in this study in 2D and 3D to examine how certain nozzle design modifications impact on the gas flow behavior and powder particle velocity variation and distribution. Meanwhile, an extended study explores the effect of particle size and process gas type. The study is strengthened by state-of-the-art experimental measurements of particle size and their associated in-flight velocities. The particle exit velocity is directly related to the deposition efficiency in the application of cold spray, and therefore acts as a useful indicator for industrial application. Through such investigations a thorough understanding of the fluid dynamic processes and the intricate interactions between the process gas and powder particles can be built enabling more quantitative control of the cold spray process.

2. Model Description

2.1 Model Overview

An axisymmetric view of the cold spray nozzle and exterior region is illustrated in Fig. 1, which summarizes the boundary conditions applied to the 3D computational model. The geometric parameters for the baseline model are provided in Table 1, which are based on a working circular cross-section cold spray nozzle, as published in

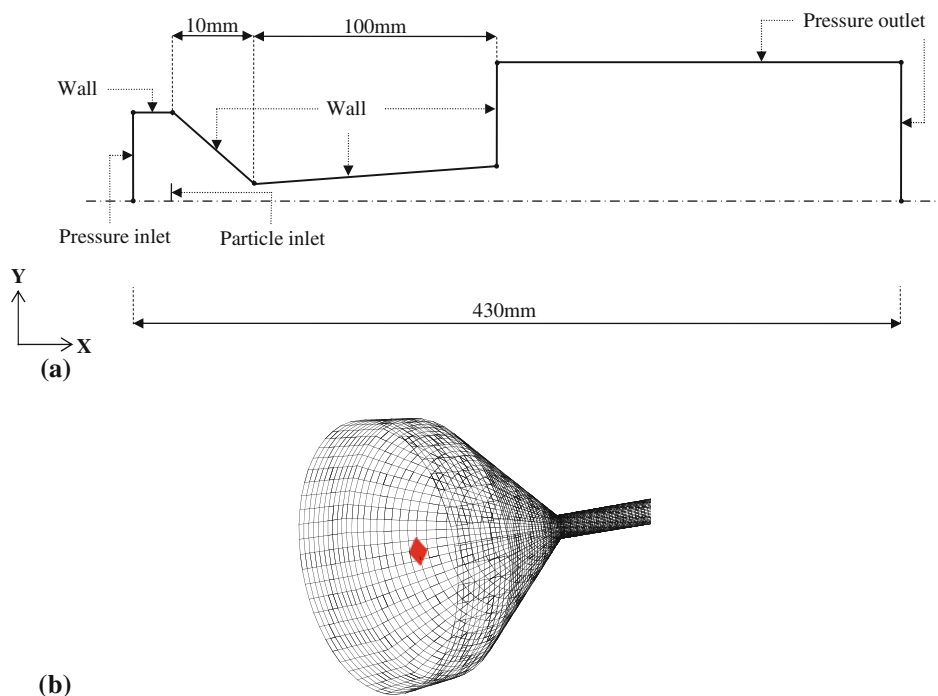


Fig. 1 An axisymmetric view of the computational boundary conditions (a) and the 3D particle inlet surface (b)

Ref 17. The experimental methodology incorporated in this study is outlined in section 3.

For the 3D simulations, the powder particles are introduced into the computation domain via a $1 \times 1 \text{ mm}^2$ region as shown in Fig. 1. Figure 2 exhibits the computational grid around the gas inlet, the de Laval nozzle throat and at the nozzle exit. The grid around the nozzle throat and the free jet region is refined to accurately capture steep variations in flow properties due to the compressible

nature of the flow. A grid sensitivity analysis was carried out whereby the grid was successively refined by increasing the number of computational cells until the magnitude of the axial velocity through the nozzle changed by less than 1% when compared to the previous refinement. This process deemed a total of 800,000 computational cells to be adequate.

The commercial finite-volume CFD package Fluent 6.3 (Fluent, Inc, Lebanon, NH, USA) is used to model a steady state compressible gas flow with discrete phase particles. The inlet and exterior regions are modeled using pressure boundaries. A nonslip condition is applied at the nozzle wall surface, which is also treated as adiabatic.

To avoid strong coupling between the pressure and velocity the pressure-based segregated solution algorithm is applied (Ref 18), whereby the solution variables (velocity components, pressure, temperature, turbulence scalars) are solved one after another. The velocity and pressure are coupled using the semi-implicit method for

Table 1 Baseline model geometric parameters

Geometric parameter	Length, mm
Throat diameter	1.35
Nozzle entrance diameter	13
Nozzle exit diameter	4
Length of converging section	10
Length of diverging section	100

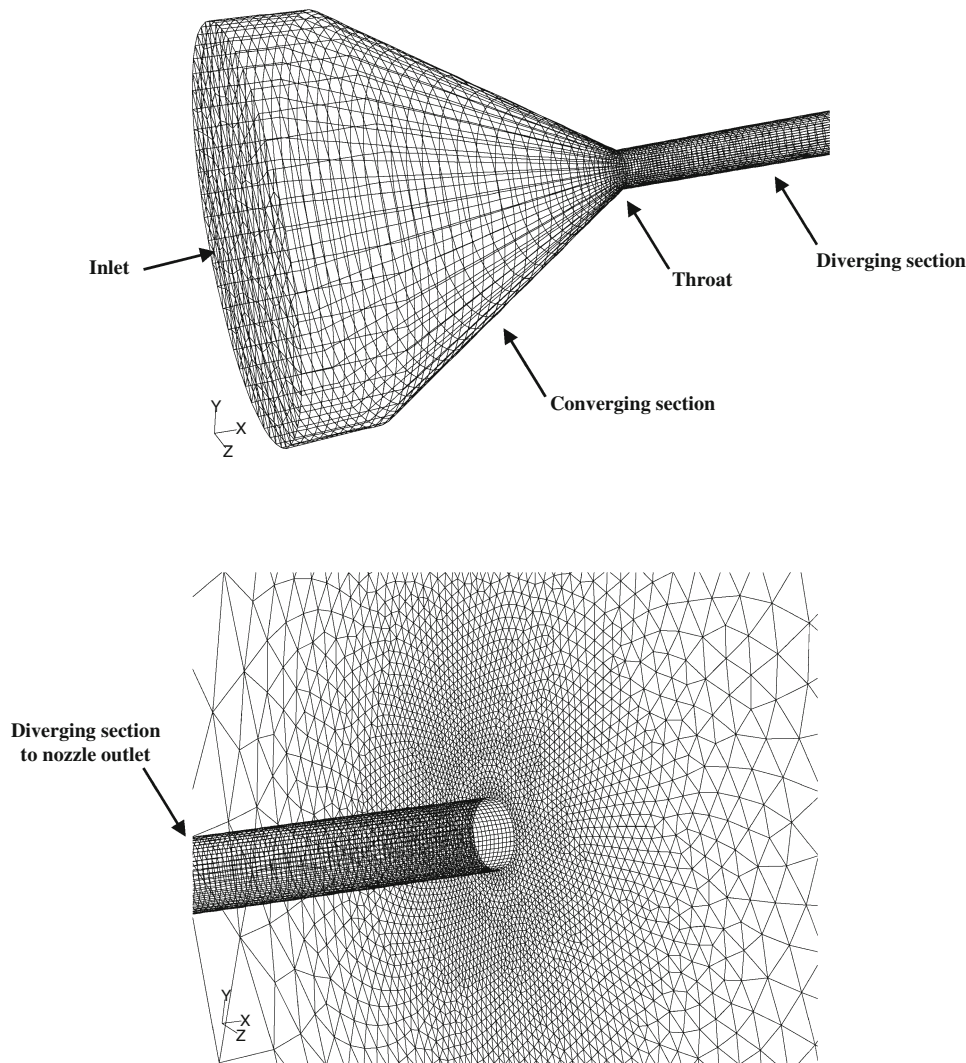
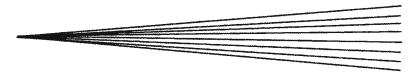


Fig. 2 Illustration of the computational grid for the converging section, the throat, and the nozzle exit



pressure linked equations (SIMPLE) algorithm (Ref 19, 20), which obtains an estimate of the pressure field using a guess and correct procedure. The transport equations are discretized using a second-order accurate upwind scheme.

Turbulence is accounted for by the k - ϵ model, which introduces a boussinesq-type turbulent viscosity in the Navier-Stokes equations. However, the standard k - ϵ model fails to accurately predict the spreading rate of an axisymmetric planar jet, which is thought to originate within the equation of turbulent dissipation (Ref 21). The realizable k - ϵ model (Ref 21) addresses this issue by introducing a modified transport equation to describe the rate of turbulent dissipation. The realizable model is also made physically more realistic by making C_μ a variable as described by Eq 1, where A_0 and A_s are constants. k is the turbulent kinetic energy of the gas phase (m^2/s^2), ϵ is rate of dissipation of the turbulent kinetic energy (m^2/s^3), and U is the free stream velocity (m/s). C_μ is then used to calculate the turbulent viscosity μ_t in Eq 2, in the same manner as the standard k - ϵ model, where ρ_g is the gas density (kg/m^3). Due to its added benefits the realizable k - ϵ model is adopted in this investigation.

$$C_\mu = \frac{1}{A_0 + A_s \left(\frac{kU}{\epsilon} \right)} \quad (\text{Eq 1})$$

$$\mu_t = \rho_g C_\mu \frac{k^2}{\epsilon} \quad (\text{Eq 2})$$

The discrete phase particle history is computed in a Lagrangian reference frame by coupling the properties of the fluid at the cell in which the particle resides with those of the instantaneous particle properties.

2.2 Discrete Phase Model

The trajectory of spherical copper (Cu) particles is simulated and the material properties are summarized in Table 2. The discrete phase particles are injected into the domain at the convergent-divergent nozzle using an artificial surface, as illustrated in Fig. 1. The trajectory of each particle is calculated using Newton's second law, equating the inertia of each particle with the forces applied by the continuum. As outlined in Ref 22, in particle-laden flows where M_r exceeds 0.6 shock patterns form on the micro-sized particles. Therefore, the calculation of the particle drag force in cold spray should include both Re_r and M_r terms, and not just Re_r as often applied. For this reason the drag force coefficient is calculated using the model proposed by Henderson (Ref 23).

The drag correlation by Henderson can be cross referenced to simulation results of supersonic flow around a

sphere (Ref 24, 25), showing a good level of concordance. These comparisons, as well as its widespread use in the application of cold spray modeling gives confidence to its use in this instance.

During the experimental procedure for measuring particle velocity-size relationship (see section 3) the particles were fed into the system at a mass flow rate of 30 g/min. At this rate the volume fraction of the powder within the gas phase is less than 10-12% and therefore it is reasonable to simulate each powder particle in a Lagrangian fashion, as a single, inert point in space with collisions between particles neglected. The momentum coupling parameter, Π_{mom} , as outlined by Eq 3-5, is used to assess the impact of the momentum of the dispersed powder on the gas phase, where ρ_d is the particle density (kg/m^3), d is the particle diameter (m), μ_c is the continuous phase viscosity ($\text{Pa} \cdot \text{s}$), U is the continuous phase velocity (m/s), L is the characteristic length (m) (i.e., the diameter of the nozzle at a specific location), and Z is the mass ratio of powder to gas.

$$\Pi_{\text{mom}} = \frac{Z}{St_{\text{mom}} + 1} \quad (\text{Eq 3})$$

$$St_{\text{mom}} = \frac{\tau_v U}{L} \quad (\text{Eq 4})$$

$$\tau_v = \frac{\rho_p d^2}{18\mu_c} \quad (\text{Eq 5})$$

This parameter has been calculated for both nitrogen and helium, and is less than 5% in all cases. Therefore, the small reduction in momentum for the gas phase due to the presence of the powder is not included in this investigation. However, if the powder flow rate was increased and Π_{mom} exceeded 0.1 (≈ 60 g/min) then one should couple the momentum of the two phases in a two-way manner. The vertical displacement induced by gravity on the discrete phase particles is deemed negligible due to the short time required by the particles to traverse the domain. Furthermore, by omitting the gravitational force the dispersion of the particles is solely influenced by the fluid dynamic behavior of the process gas flowing through the designed nozzle. A thermophoretic force is included which arises due to temperature gradients within the flow. All the discrete particles remain spherical and therefore the drag force model does not change accordingly. All discrete particles are identical at the inlet, with the same diameter, temperature, and inlet velocity, which is perpendicular to the inlet surface, and parallel to the x -axis.

The dispersion of the particles is accounted for by computing the trajectory of each particle based on the sum of the mean and turbulent velocity component of the gas phase in all three coordinate directions. For example, the velocity components in the x -direction are shown in Eq 6. Due to the assumption of isotropic turbulence the root mean square (RMS) of each fluctuating component (u' , v' , and w') of the gas phase are equal, and are deduced from the turbulent kinetic energy, k , of the gas phase through Eq 7. The values u' , v' , and w' are sampled assuming they

Table 2 Summary of simulated powder material

Property	Description
Material	Inert gas atomized copper (Cu)
Particle density, kg/m^3	8978
Specific heat capacity, $\text{J}/\text{kg}/\text{K}$	381
Initial particle velocity, m/s	20
Initial particle temperature, K	300

obey a Gaussian (normal) probability distribution and are deduced by Eq 8. ζ is a random number selected from a Gaussian (normal) distribution.

$$u = \bar{u} + u' \quad (\text{Eq 6})$$

$$\sqrt{u'^2} = \sqrt{v'^2} = \sqrt{w'^2} = \sqrt{2k/3} \quad (\text{Eq 7})$$

$$u' = \zeta \sqrt{u'^2} \quad (\text{Eq 8})$$

Several groups of particles enter the domain at several points at the particle inlet surface, and the number of particles per group represents the number of tries used by the probability-based solver to compute the random effects of turbulence on the discrete particles. Therefore, by increasing the number of particles per group the dispersion accuracy can be increased.

The integral time scale, T_L , is estimated by Eq 9, where k is the turbulent kinetic energy (m^2/s^2) and ε is the rate of turbulent kinetic energy dissipation (m^2/s^3). The characteristic lifetime of an eddy, τ_e , is specified in Eq 10 and the eddy crossing time, t_{cross} , is given by Eq 11, where L_e is the eddy length scale, τ is the particle relaxation time, and $|u - u_p|$ is the magnitude of the relative velocity between the particle and gas phase. Equation 12 gives the particle relaxation time, where μ is the gas viscosity, d_p is the particle diameter, and ρ_p is the particle density.

$$T_L = 0.15 \frac{k}{\varepsilon} \quad (\text{Eq 9})$$

$$\tau_e = 2T_L \quad (\text{Eq 10})$$

$$t_{\text{cross}} = -\tau \ln \left(1 - \frac{L_e}{\tau |u - u_p|} \right) \quad (\text{Eq 11})$$

$$\tau = \frac{\rho_p d_p^2}{18\mu} \quad (\text{Eq 12})$$

A simulated particle is assumed to be in contact with the turbulent eddy for the shorter of the eddy lifetime (Eq 10) and eddy crossing time (Eq 11). At the end of this time, a new turbulent velocity fluctuation (u') is generated based on a new random value of ζ and the total velocity (u) is updated. The total velocity is constant over the solution advancement time step Δt and the value of Δt is estimated so that the trajectory of each discrete particle is carried out five times as it traverses a computational cell.

The trajectory calculation is an integration of the force balance on the particle as given in Eq 13 (in the x -direction). In this equation, u_p is the particle velocity, u is the gas phase velocity, Re_p is the Reynolds number based on the particle diameter, F_x is a source term which in this instance represents the thermophoretic force, and C_D is determined by the drag coefficient from Henderson (Ref 23).

$$\frac{du_p}{dt} = \frac{18\mu}{\rho_p d_p^2} \frac{C_D Re_p}{24} (u - u_p) + F_x \quad (\text{Eq 13})$$

3. Experimental Methodology

3.1 Cold Spray Equipment

CGDS was carried out at The University of Nottingham using an in-house designed system which is described in detail in a previous paper (Ref 26). A de Laval nozzle of dimensions identical to that given in Table 1 was employed. Nitrogen was used as the carrier gas for the powder which was fed axially into pre-chamber of the nozzle as illustrated schematically in Fig. 3. Normally, room temperature helium is used as the main processing gas to produce cold sprayed deposits. However, in this study, involving a comparison with CFD calculations, experiments were performed with both room temperature nitrogen and room temperature helium as process gases at 29-bar stagnation pressure. When carrying out the particle sizing and velocity measurements as described in section 3.2, the de Laval nozzle was operated in a horizontal plane without the presence of a substrate.

A high pressure powder feeder (1264HP, Praxair, USA) was employed with a “120-hole” feed wheel and a wheel speed of 4 rpm which gave a powder feed rate for the copper powder employed of approx 30 g/min. The copper powder was inert gas atomized with a nominal size range +5 to -25 μm (Sandvik Osprey Ltd, Neath, UK) and had a near-spherical morphology.

3.2 Methodology for Particle Size and Velocity Measurements

Particle velocities and diameters were measured by a technique called Particle/Droplet Image Analysis or PDIA using the VisiSizer system produced by Oxford Lasers (Oxford Lasers, Didcot, UK). The principles of operation of the system, shown schematically in Fig. 3, are as follows. An axial section of the spray plume is back lit (shadow graph method) for a short period (~6 ns) by a diffused, pulsed Nd:YAG laser light (532 nm) and two consecutive images are captured by a digital camera with an image separation time of typically 200 to 300 ns. Image processing software (VisiSizer v2.09, Oxford Lasers, Didcot, UK) employs a cross correlation algorithm to pair particles together. Using a known camera magnification and a known time delay between image frames individual particle velocities and corresponding particle diameters can be calculated. In this study, a field of view (FOV) of $1134 \times 1134 \mu\text{m}$ was employed. Using this system it was possible to accurately measure particles as small as 3 μm in diameter. The image processing software was set to reject particles that failed to meet shape or focus criteria and so eliminate spurious data from overlapping particles or particles not within the measurement plane, i.e., the plane of focus. The depth of field of the system was around 1 mm under the imaging conditions of operation in this study so data obtained will approximate very closely to only those particles travelling along the spray plume axis.

For each experimental run, data were recorded so that measurements of diameter and corresponding velocity

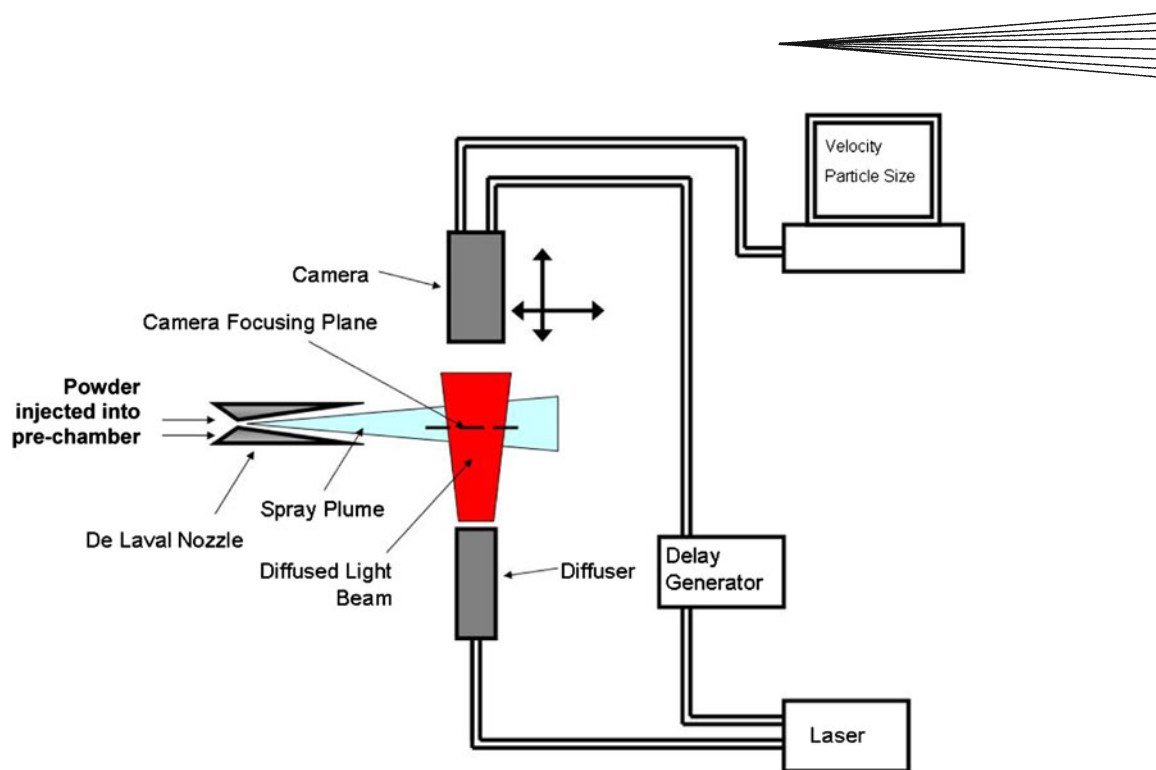


Fig. 3 Schematic illustration of particle droplet image analysis system

could be obtained from 500 individual particles at a stand-off distance of 20 mm from the nozzle exit and along the central axis of the spray plume. Further details of the experimental methodology are reported elsewhere (Ref 27).

4. Results and Discussion

4.1 Measurements of Particle Size and Velocity

In order to assess the accuracy of the size measurements performed by PDIA, in situ, in the spray plume the resultant size distribution of the 500 measured particles was compared with that of the original copper powder feedstock. The size distribution of the original feedstock was determined by a standard laser diffractometry (LD) method. Both the PDIA and the LD data were found to closely fit a log-normal size distribution which is typically to be expected from a gas atomized powder. The PDIA method gave a mean value for the diameter of 7.3 μm with a standard deviation for the log-normal distribution of 4.5 μm which compares very well with the LD measurements of 6.7 and 4.6 μm , respectively, for mean diameter and standard deviation of the log-normal distribution. Figure 4(a) and (b) shows scatter plots of particle velocity, V , and diameter, D , for 500 valid particles with N_2 and He process gas, respectively, at 29-bar stagnation pressure. Due to the small number of larger particles in the powder the data points are seen to become sparsely populated as the particle diameter increases. Clearly, there is a wide spread of particle velocities for particles of the same diameter and similar scatter is typically observed in

diagnostic measurements of plasma spray or high velocity oxy-fuel spray plumes (Ref 28).

The raw particle data shown in Fig. 4 were ordered by increasing diameter and grouped into bins, each comprising 20 particles. For each bin the mean particle size and velocity were computed and the results obtained are shown in Fig 5. In this plot, the error bars represent the standard error in the mean of the velocity data, i.e.,

$$\frac{\sigma}{\sqrt{N}}$$

where σ is the standard deviation of the velocity data in the bin and N is the number of data values in the bin (in all cases 20).

It is clear that for all particle diameters He, as a process gas, produces particle velocities around twice that of nitrogen. Also the stagnation pressure of 29 bar has been shown previously to produce significantly higher particle velocities than 10, 20, or 25 bar (Ref 27). It is apparent that, particularly in the case of He as a process gas, particle velocity has decreased for bin sizes in the range 5 to 8 μm at a stand-off distance of 20 mm which is somewhat unexpected. This could be due to either these small particles decelerating outside the de Laval nozzle or failing to be accelerated to the expected velocity inside the nozzle. To test this, a limited number of measurements were performed at a 1 mm stand-off distance and a similar effect was observed. Thus, it would seem possible that these smaller particles more readily diverge from an axial trajectory when injected into the de Laval nozzle than do larger particles of greater mass. They thus experience lower than optimum acceleration as discussed further in section 4.4.

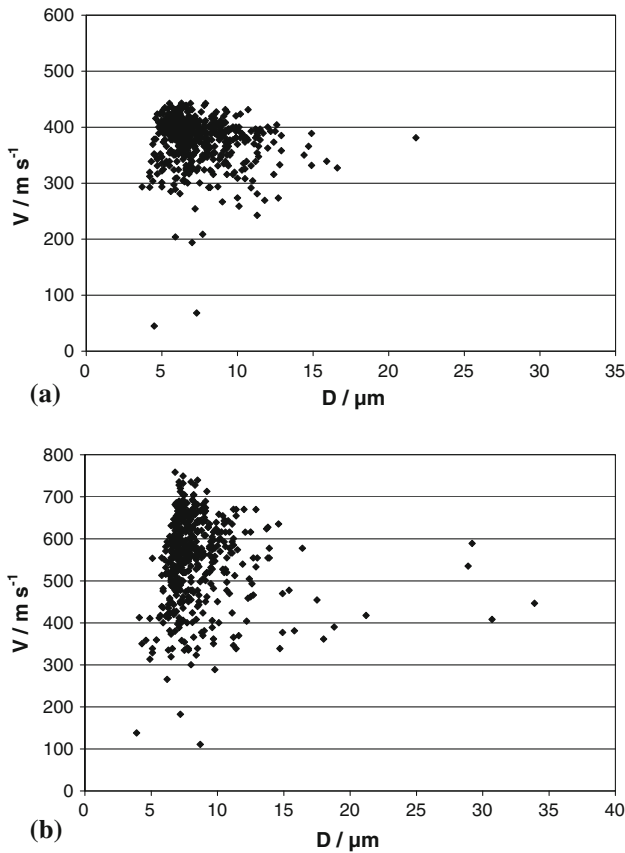


Fig. 4 Scatter plot of particle velocity versus diameter using (a) N_2 process gas and (b) He process gas at 29 bar, 293 K and a stand-off distance of 20 mm

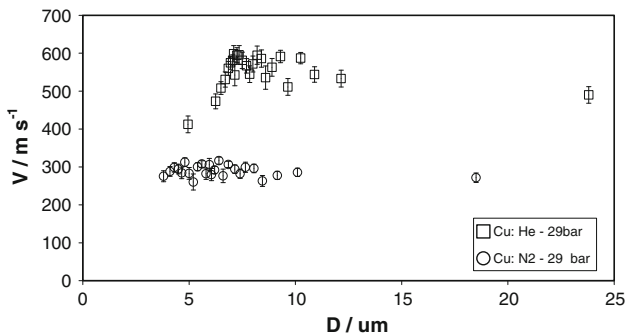


Fig. 5 Plot of mean particle velocity versus particle diameter for particles grouped in bin sizes of 20 particles

4.2 Comparison Between Experimental Measurements and Baseline Calculations

From the PDIA results, the maximum particle velocity for a number of particle diameters is used in this investigation for comparison with the simulation results. An SEM image of the Cu particles is exhibited in Fig. 6, justifying the use of a spherical-based drag model.

The baseline geometry for the simulations is outlined in Table 1 and the inlet boundary stagnation pressure is

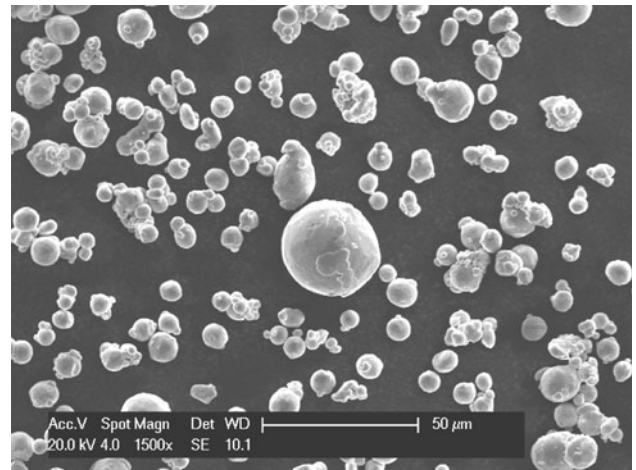


Fig. 6 SEM image of copper powder used in the experimental section of this study

29 bar. In order to replicate the maximum velocity a single particle is simulated, travelling along the centerline of the computational domain. The simulation is repeated for helium and nitrogen process gases, and for several different particle diameters. The simulated particle velocities at a stand-off distance of 20 mm are compared with the experimental measurements at a stand-off distance of 20 mm, as illustrated in Fig. 7. The comparisons show a similar trend, where the particles decrease in velocity with an increase in size. However, the simulations over-predict the velocities by roughly 50 and 200 m/s for nitrogen and helium process gases, respectively. These discrepancies are believed to be caused by the assumption of a one-dimensional trajectory along the centerline, where the process gas velocity is optimum. In reality, each particle will travel at varying angles away from the centerline at the inlet and therefore will not be located along the centerline throughout their trajectory, where the process gas velocity and drag force is lower.

4.3 Nozzle Cross Section Shape

The effect of the cross-sectional shape of the cold spray nozzle on the particle velocity and distribution at the exit is numerically tested by introducing roughly 1000 Cu particles (11 μm in diameter) from the region shown in Fig. 1 into the computational domain, carried by nitrogen at a stagnation pressure of 29 bar and 298 K. Each cross-sectional shape: circular, square, and elliptical are investigated by designing the wall shape from the inlet to the exit of the de Laval nozzle, each with the same varying cross-sectional area along the axis.

Figure 8(a) depicts the velocity of each particle against its radial distance from the centerline at the exit of each investigated nozzle. For the elliptical and square cross-sections, the radial location of each particle is plotted independently of its Y-Z coordinate. The Y-Z coordinates for each particle at the exit of each nozzle are exhibited in Fig. 8(b). The results show that for all nozzle types the particles are distributed around centerline axis. The circular

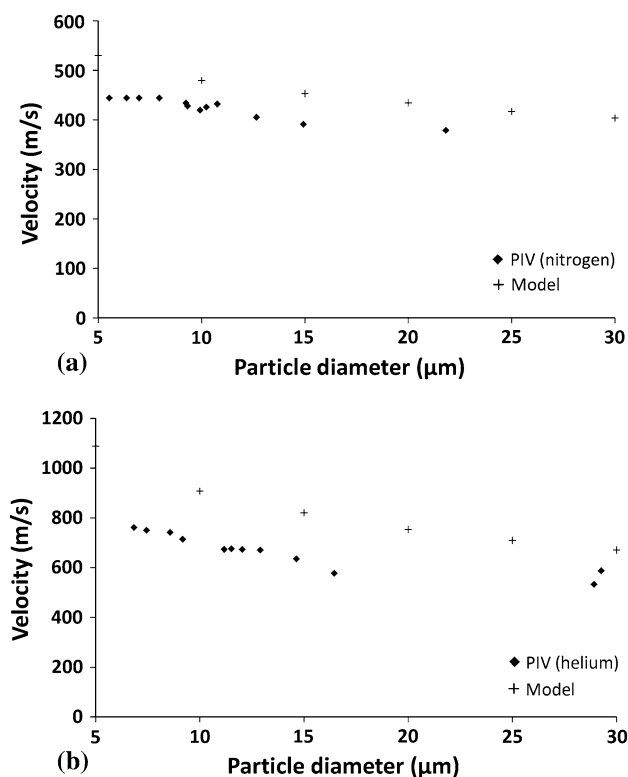


Fig. 7 Comparison between the simulated and the PIV measured particle velocities with (a) nitrogen process gas and (b) helium process gas at a SOD of 20 mm

cross section and square cross section produce the least distributed set of particles in terms of both their radial position from the centerline and their nozzle exit velocity. For these two nozzles 99% of the particles are within the 460–465 m/s range as summarized in Table 3. The results in Table 3 also show the wider range of particle velocity created by the elliptic cross section. The results show that roughly 20% fall below 460 m/s, and of these, a further 3% exit at a velocities less than 450 m/s. The correlation between the particle velocity and Y - Z location at the nozzle exit of the elliptic nozzle is depicted in Fig. 8(b). A clear decrease in velocity and increased dispersion occurs with increasing distance along the Z -axis from the center. A steeper velocity gradient between the wall and the center of the flow is present in the Z -direction compared to the Y -direction due to the shorter distance, creating greater shear stresses within the flow. As a result an increase in turbulent kinetic energy and resulting velocity fluctuations arise leading to a noticeable dispersion of the particles in the Z -direction. The particles which are displaced toward the wall experience a decrease in drag force due to the decreasing flow velocity toward the wall resulting in a lower exit velocity.

4.4 Particle size and Process Gas

The effect of the particle size on the particle velocity and displacement distribution at the exit of the nozzle is tested by comparing 5 and 30 μm particles. 1000 particles

are introduced into the conical nozzle computational domain, and are carried by nitrogen gas at a stagnation pressure of 29 bar and 298 K.

Figure 9 shows the modeled variation in the displacement and velocity distributions at the exit of the de Laval nozzle, for a 5 and a 30 μm powder source. The 5 μm particles are clearly more dispersed by the expanding gas phase and turbulent fluctuations. On the other hand, 30 μm particles are less easily affected, which results in a more confined dispersion pattern with significantly slower velocities at the exit of the nozzle. While the variation in velocity for the smaller particles is larger, the velocity for all 5 μm particles remains superior throughout compared to the larger 30 μm particles.

Nitrogen and helium process gases are compared at a stagnation pressure of 29 bar and 298 K. 1000 11 μm Cu particles are introduced into the computational domain. Figure 10 shows the extent by which the helium velocity greatly exceeds the nitrogen gas velocity along the centerline. The results in Fig. 10 and 11 show that helium gas is far more effective at accelerating the powder particle than nitrogen. Helium is also shown to disperse the powder particles in Fig. 11 more than nitrogen. This is due to the higher levels of turbulence found in the helium flows which are induced by the higher velocity gradients through the fluid. The turbulent velocity fluctuations are estimated using Eq 7 and quantified by Fig. 12 at the exit of the conical nozzle for nitrogen and helium process gases.

4.5 Contoured Nozzle

The straight edge of the original baseline nozzle is contoured by applying the MOC. A MatLab code (Nozzle Design Program by means of MOC, University of Southampton) is used to create an axisymmetric minimum length nozzle. A contour correction is also included which makes the model applicable to viscous flow. The nozzle wall is corrected by a distance equal to the displacement thickness of the wall boundary layer. The semi-empirical method for the calculation of compressible turbulent boundary layers published by Tucker (Ref 29) is applied and converted to an axisymmetric domain using the methods presented in Ref 30. This contour is designed so that the stagnant nitrogen gas at a pressure of 30 bar and temperature of 300 K is expanded to a steady state supersonic flow which is free of shocks inside the expanding section. First, this technique is applied to create a nozzle with the same geometric properties as the baseline model, with an outlet diameter of 4 mm. The contour shape is exhibited in Fig. 13. In order to create the same expanding-section length as the baseline model a barrel is attached to the end of the minimum length nozzle. This length is required to give the powder particles a sufficient amount of acceleration time inside the high speed gas.

Figure 14 summarizes the simulated gas flow and resulting in single 11 μm Cu particle velocity along the centerline for the baseline model and contoured designs. For the original conical nozzle, the compressed nitrogen is forced through the de Laval nozzle, at the throat the flow is choked at mach one and the nitrogen gas velocity is

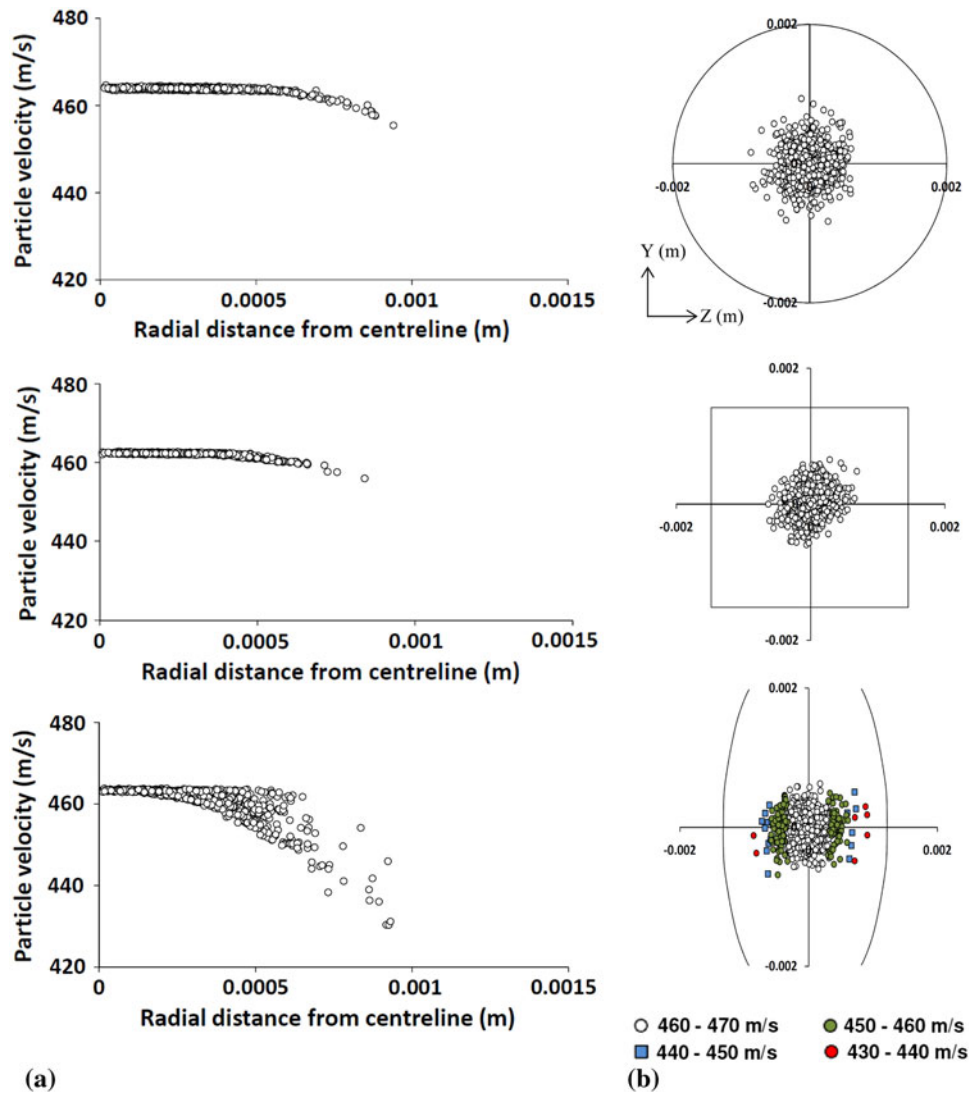


Fig. 8 Relationship between particle velocity and radial distance (a) and exit distribution (b) at the exit of each simulated nozzle cross-sectional shape

Table 3 Cumulative percentage of particles with increasing exit velocity for the three tested cross sections

Velocity limit, m/s	Percentage of particles with velocity < velocity limit		
	Circular	Square	Elliptical
430	0.00	0.00	0.00
435	0.00	0.00	0.35
440	0.00	0.00	0.82
445	0.00	0.00	1.41
450	0.00	0.00	2.71
455	0.00	0.00	7.53
460	1.00	1.11	21.06
465	100.00	100.00	100.00

raised slowly and smoothly through the expansion section, with the exception of some small oscillation in the flow close the critical section of the nozzle. The gas velocity

reaches a maximum velocity at the exit of the nozzle. At this point the gas pressure is lower than the atmospheric pressure resulting in an over-expanded flow regime at the exit, characterized by a sharp decrease in velocity at the nozzle exit. The lower gas pressure of the exhausting nitrogen in comparison to the atmospheric pressure leads to the exhaust gas being compressed inwards resulting in an increase in exhaust gas pressure. However, the flow is naturally over compressed to a pressure greater than the atmospheric pressure, which then causes the gas to expand. Mixing of the exhaust gas with the atmosphere occurs in the stand of region and the process of over compression and over expansion continues until the exhaust gas pressure reaches the same value as the atmospheric pressure. The oscillations are clearly visible in the modeled results, shown in Fig. 14. Furthermore, the over-expanded flow regime at the nozzle exit is exhibited in Fig. 15 in terms of gas velocity and density variation.

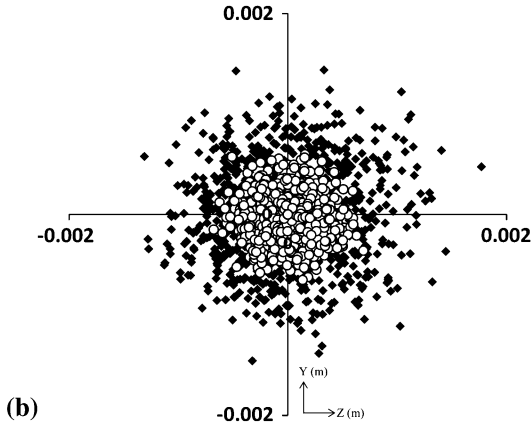
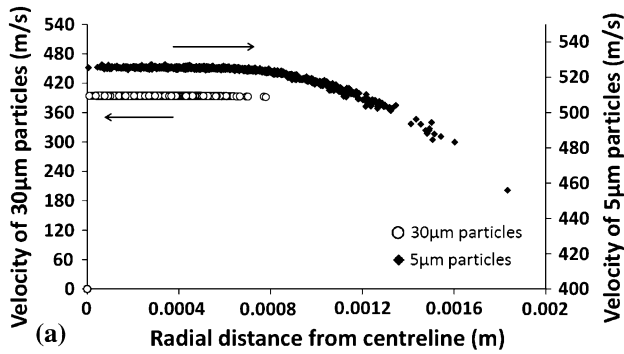


Fig. 9 Comparison of particle velocity variations (a) and particle distributions (b) at the exit of the baseline nozzle for 5 and 30 μm Cu particles

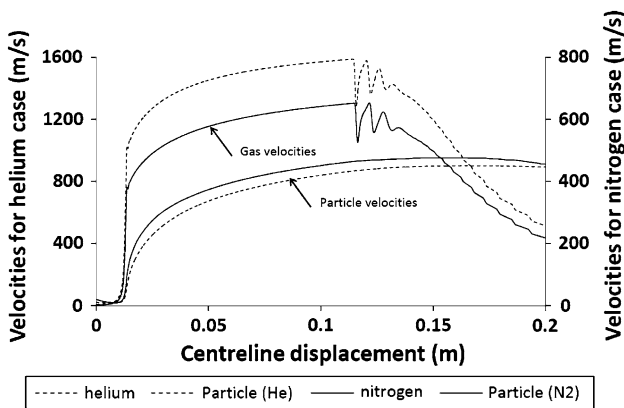


Fig. 10 Comparison of gas and 11 μm Cu particle velocities through the baseline geometry for helium and nitrogen process gases

Over-expanded jet phenomena are commonly found in thermal spraying. A good example of experimental images of such regimes can be found in Ref 31. Further details on this flow regime can be found in Ref 32.

Owing to the same throat and exit diameter the exit velocity and exterior jet region of the contour design and the conical baseline model are very similar, with an over-expanded flow region. However, for the contoured nozzle,

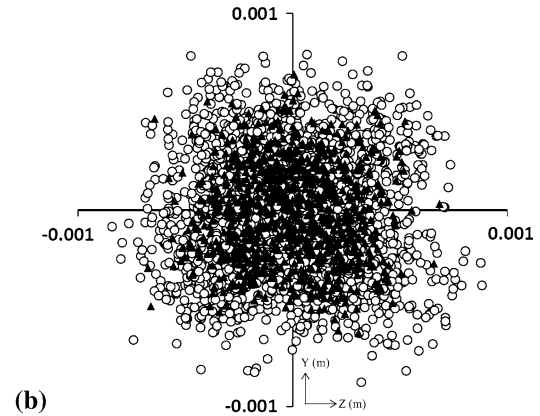
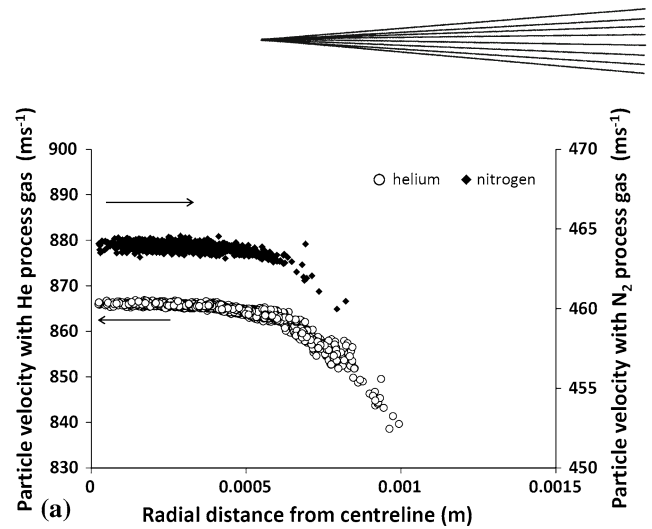


Fig. 11 Comparison of particle velocity variations (a) and particle distributions (b) at the exit of the baseline nozzle for helium and nitrogen process gases

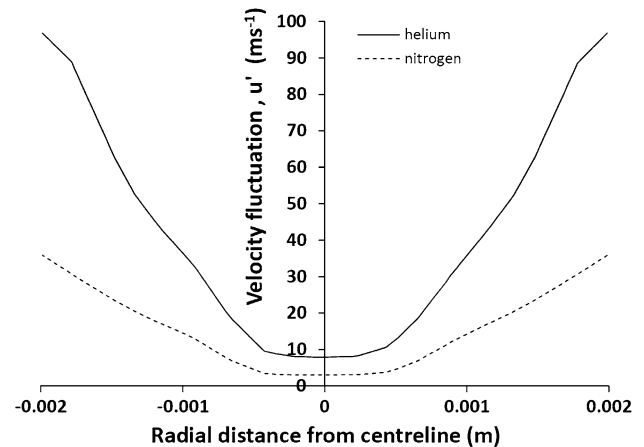


Fig. 12 Comparison of turbulent velocity fluctuations at the exit of the conical nozzle for nitrogen and helium process gases

the flow is accelerated rapidly when exiting the throat and the velocity profile for this design remains higher than the conical design throughout the expanding and barrel section of the de Laval nozzle. While the designed contour section creates a smooth, shock-free flow through the expanding section of the nozzle, oscillations occur along

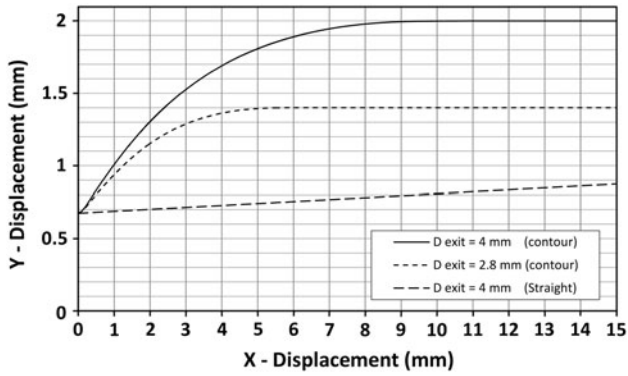


Fig. 13 Close up of the compared expansion sections illustrating the different expanding minimum length contour designs over 15 mm of the 100 mm total throat to exit length

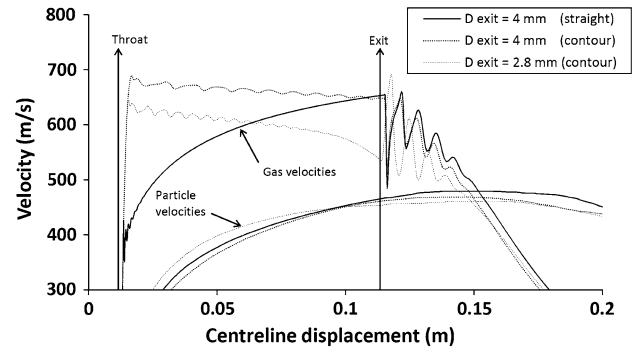


Fig. 14 Gas and particle velocities through the baseline and contoured nozzle geometries

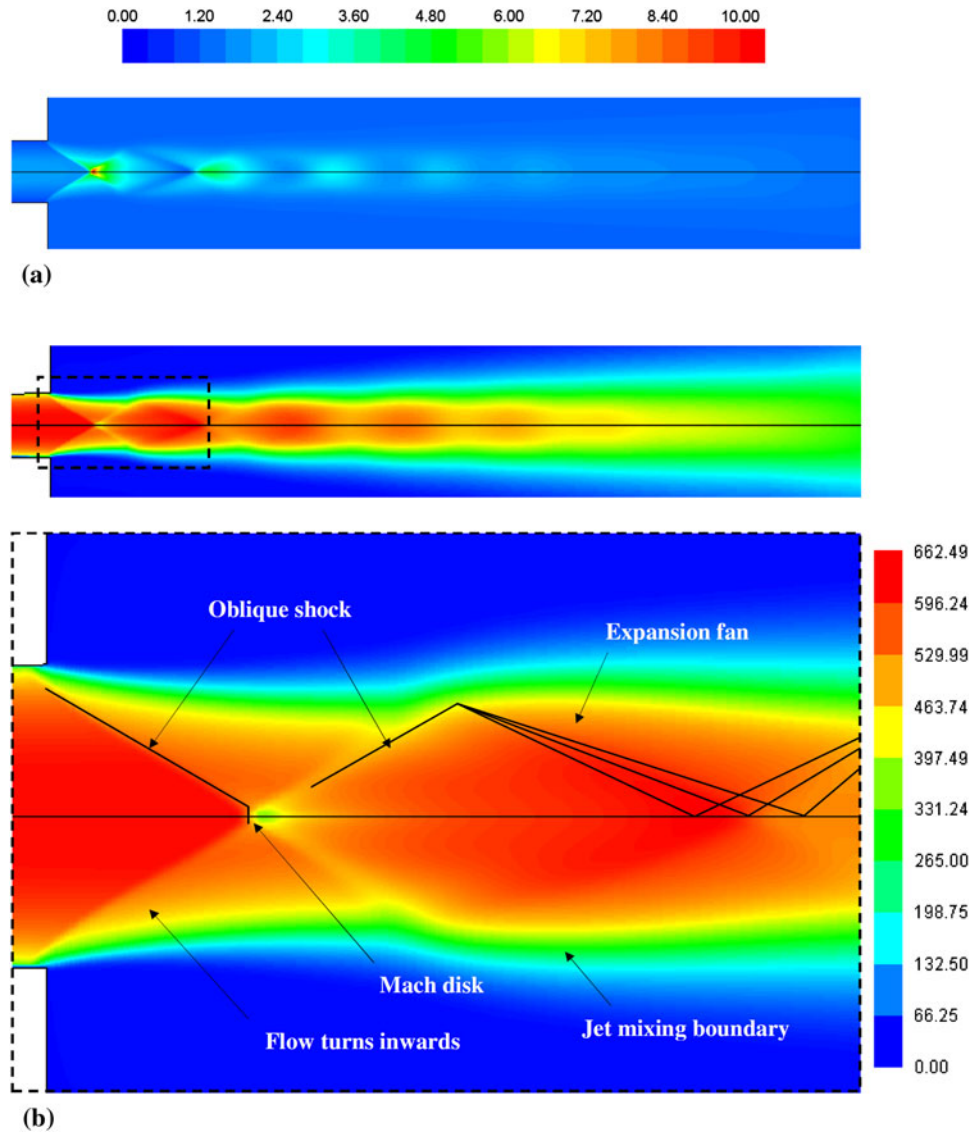


Fig. 15 Density contours (kg/m^3) (a) and velocity contours (m/s) (b) at the exit of the nozzle showing the over-expanded flow regime



the barrel due to strong reflections at the internal surface. This rapid increase in velocity of the process gas in the minimum length nozzle leads to a decrease in density and static pressure. For the contour nozzle, the decrease in density during the rapid acceleration and expansion of the process gas results in lower particle acceleration through the system compared to the conical design, leading to a slightly lower particle velocity at the exit and within the stand-off region, as exhibited in Fig. 14. This difference in particle velocity may be viewed as negligible, and the use of a minimum length nozzle and barrel extension may be seen as equivalent to a long diverging section. As a result, if the manufacture of the long diverging nozzle proves difficult then one may produce a minimum length nozzle with an attached constant diameter barrel of appropriate length.

The exit diameter of the minimum length nozzle was reduced incrementally with the same barrel attached. The results showed that for a contoured design with an exit diameter of 2.8 mm the process gas is expanded less, leading to a lower velocity. However the density remains higher creating a faster particle velocity profile along the first half of the barrel section. In this case, the gas velocity begins to decrease along the barrel due to the over expansion, indicating that the barrel length is crucial in the design of the minimum length nozzle. As a result the particle acceleration depletes, resulting in a lower exit velocity when compared to the baseline conical design. By further decreasing the diameter of the nozzle exit the flow is choked inside the barrel, leading to a degraded and inefficient flow regime.

5. Conclusion

Compressible, supersonic nitrogen, and helium gas flow is simulated in 2D and 3D through a cold spray convergent-divergent nozzle. Cu particles of various diameters are coupled in a Lagrangian reference frame, and their resulting dynamic response is investigated with the inclusion of turbulent effects. The results drawn from this investigation are summarized below:

- The effect of the cross-sectional shape of the cold spray nozzle on the particle velocity and distribution is tested for nitrogen at stagnation pressure of 2.9 MPa and copper particles of 11 μm diameter. The results show that relative to the elliptical cross section, the circular and square cross sections have the least dispersed powder distribution as well as the greatest average particle velocities. Therefore, a circular or square cross section should be selected to achieve the very highest particle velocities. However, the velocity reduction within the elliptical flow is relatively small, at a maximum of roughly 20 m/s. A more dispersed particle flow is advantageous for the build up of an evenly distributed coating. In these cases an elliptical shape is most beneficial.
- Furthermore, the effect of the particle size on the particle velocity and displacement distribution at the

exit of the nozzle is tested. The 5 μm particles are more dispersed and have higher velocities at the exit when compared to the 30 μm particles.

- Helium is shown to disperse the powder particles more than nitrogen due to the higher levels of turbulence created by the helium gas flow.
- A contoured shape is created for the diverging section of the nozzle with a minimum length using the MOC. A barrel of constant diameter is then added to the exit. The simulated gas and particle velocities are then compared to the original conical design, with the same throat and exit diameter and throat to exit length. The gas flow in this contoured nozzle is accelerated rapidly and the velocity profile remains higher than the conical design throughout the expanding section of the de Laval nozzle. However, due to a decrease in gas density a slightly lower particle velocity is observed for the minimum length MOC nozzle design at the exit and within the stand-off region. However, this difference is negligible and therefore one may alternatively produce a minimum length nozzle with an attached barrel of appropriate length.

Measurements of particle size and corresponding velocity have been recorded and the results show a similar trend to the simulation results. The particle velocities are over-predicted by the simulation by roughly 50 m/s for a nitrogen process gas, and by roughly 200 m/s for a helium process gas. The over-predicted velocity is believed to be down to an idealistic comparison with a particle travelling along the centerline. Future study should sought to investigate the correlation between particle inlet conditions and their resulting velocity profile.

Acknowledgments

The authors would like to thank Dr Zhiwei Hu (Reginald Platt Lecturer in Civil Aviation, University of Southampton) for providing a program for computing the method of characteristics. The authors gratefully acknowledge the financial support from the EC FP7 Simuspray project (Grant No. 230715).

References

1. A. Papyrin, V. Kosarev, S. Klinkov, A. Alkhimov, and V.M. Fomin, *Cold Spray Technology*, Elsevier, Amsterdam, 2007
2. R.C. Dykhuizen and M.F. Smith, Gas dynamic Principles of Cold Spray, *J. Therm. Spray Technol.*, 1998, **7**, p 205-212
3. K. Balani, A. Agarwal, S. Seal, and J. Karthikeyan, Transmission Electron Microscopy of Cold Sprayed 1100 Aluminum Coating, *Scripta Mater.*, 2005, **53**, p 845-850
4. W.Y. Li, C. Zhang, X.P. Guo, G. Zhang, H.L. Liao, C.J. Li, and C. Coddet, Effect of Standoff Distance on Coating Deposition Characteristics in Cold Spraying, *Mater. Des.*, 2008, **29**, p 297-304
5. H. Assadi, F. Gartner, T. Stoltenhoff, and H. Kreye, Bonding Mechanisms of Cold Gas Spraying, *Acta Mater.*, 2003, **51**, p 4379-4394
6. M. Grujicic, C.L. Zhao, W.S. De Rosset, and D. Helfritsch, Adiabatic Shear Instability Based Mechanism for Particles/Substrate

- Bonding in the Cold-Gas Dynamic-Spray Process, *Mater. Des.*, 2004, **25**, p 681-688
7. P.C. King, S.H. Zahiri, and M. Jahedi, Focused Ion Beam Micro-Dissection of Cold-Spray Particles, *Acta Mater.*, 2008, **56**, p 5617-5626
 8. B. Gyuyeol, Y. Xiong, S. Kumar, K. Kang, and C. Lee, General Aspects of Interface Bonding in Kinetic Sprayed Coatings, *Acta Mater.*, 2008, **56**, p 4858-4868
 9. T. Schmidt, F. Gartner, H. Assadi, and H. Kreye, Development of a Generalized Parameter Window for Cold Spray Deposition, *Acta Mater.*, 2006, **54**, p 729-742
 10. W.Y. Li and C.J. Li, Optimal Design of a Novel Coldspray Gun Nozzle at Limited Space, *J. Therm. Spray Technol.*, 2005, **14**, p 391-396
 11. W.Y. Li, H.L. Liao, H.T. Wang, C.J. Li, G. Zhang, and C. Coddet, Optimal Design of a Convergent-Barrel Cold Spray Nozzle by Numerical Method, *Appl. Surf. Sci.*, 2006, **253**, p 708-713
 12. W.Y. Li, H.L. Liao, G. Douchy, and C. Coddet, Optimal Design of a Cold Spray Nozzle by Numerical Analysis of Particle Velocity and Experimental Validation with 316L Stainless Steel Powder, *Mater. Des.*, 2007, **28**, p 2129-2137
 13. J. Pattison, S. Celotto, A. Khan, and W. O'Niell, Standoff Distance and Bow Shock Phenomena in the Cold Spray Process, *Surf. Coat. Technol.*, 2008, **202**, p 1443-1454
 14. T.C. Jen, L. Li, W. Cui, Q. Chen, and X. Zhang, Numerical Investigations on Cold Gas Dynamic Spray Process With Nano- and Microsize Particles, *Heat Mass Transf.*, 2005, **48**, p 4384-4396
 15. H. Katanoda, M. Fukuhara, and N. Lino, Numerical Study of Combination Parameters for Particle Impact Velocity and Temperature in Cold Spray, *J. Therm. Spray Technol.*, 2007, **16**, p 627-633
 16. M. Karimi, A. Fartaj, G. Rankin, D. Vanderzwet, W. Birtch, and J. Villafuerte, Numerical Simulation of the Cold Gas Dynamic Spray Process, *J. Therm. Spray Technol.*, 2006, **15**, p 518-523
 17. T.S. Price, P.H. Shipway, D.G. McCartney, E. Calla, and D. Zhang, A Method for Characterizing the Degree of Inter-particle Bond Formation in Cold Sprayed Coatings, *J. Therm. Spray Technol.*, 2007, **16**, p 566
 18. J.P. Vandoormaal, G.D. Raithby, and B.H. McDonald, The Segregated Approach to Predicting Viscous Compressible Fluid Flows, *J. Turbomach.*, 1987, **109**, p 268-277
 19. M. Peric, Analysis of Pressure-Velocity Coupling on Nonorthogonal Grids, *Numer. Heat Transf. B*, 1990, **17**, p 63-82
 20. G.D. Raithby and G.E. Schneider, Numerical Solution of Problems in Incompressible Fluid Flow, *Numer. Heat Transf.*, 1979, **2**, p 417-440
 21. T.H. Shih, W.W. Liou, A. Shabbir, and J. Zhu, New k- ϵ Eddy-Viscosity Model for High Reynolds Number Turbulent Flows - Model Development and Validation, *Comput. Fluids*, 1995, **24**, p 227-238
 22. C. Crowe, M. Sommerfeld, and Y. Tsuji, *Multiphase Flows With Droplets and Particles*, CRC Press, Boca Raton, 1998
 23. C.B. Henderson, Drag Coefficients of Spheres in Continuum and Rarefied Flows, *AIAA J*, 1976, **14**, p 707-708
 24. M. Sun, T. Saito, K. Takayama, and H. Tanno, Unsteady Drag on a Sphere By Shock Wave Loading, *Shock waves*, 2004, **14**, p 3-9
 25. T. Saito, M. Saba, M. Sun, and K. Takayama, The Effect of an Unsteady Drag Force on a Structure of a Non-Equilibrium Region Behind a Shock Wave in a Gas-Particle Mixture, *Shock Waves*, 2007, **17**, p 255-262
 26. D. Zhang, D.G. McCartney, and P.H. Shipway, Cold gas Dynamic Spraying of Aluminum: The Role of Substrate Characteristics in Deposit Formation, *J. Therm. Spray Technol.*, 2005, **14**, p 109-116
 27. T.S. Price, "Cold gas dynamic spraying of titanium coatings," PhD Thesis, University of Nottingham, 2008
 28. L. Zhao, M. Maurer, F. Fischer, and E. Lugscheider, *Surf. Coat. Technol.*, 2004, **185**, p 160-165
 29. M. Tucker, "Approximate Turbulent boundary-layer development in plane compressible flow along thermally insulated surfaces with application to supersonic-tunnel contour correction," NACA TN 2045, 1950
 30. J.C. Sivells, Aerodynamic Design of Axisymmetric Hypersonic Wind-Tunnel Nozzles, *J. Spacecr. Rocket.*, 1970, **7**(11), p 1291-1299
 31. B. Jodoin, M. Gindrat, J.-L. Dorier, CH. Hollenstein, M. Loch, and G. Barbezat, Modelling and Diagnostics of a Supersonic DC Plasma Jet Expanding at Low Pressure, *Proceedings of ITSC 2002 International Thermal Spray Conference*, March 4-6 2002, Essen, Germany
 32. J.D. Anderson, *Fundamentals of Aerodynamics*, 4th ed., McGraw-Hill, New York, 2007, p 637